

Magnetic charges and magnetoelectricity in hexagonal rare-earth manganites and ferrites

Meng Ye* and David Vanderbilt

Department of Physics & Astronomy, Rutgers University, Piscataway, New Jersey 08854, USA

(Dated: June 16, 2021)

Magnetoelectric (ME) materials are of fundamental interest and show broad potential for technological applications. Commonly the dominant contribution to the ME response is the lattice-mediated one, which is proportional to both the Born electric charge Z^e and its analogue, the dynamical magnetic charge Z^m . Our previous study has shown that exchange striction acting on noncollinear spins induces much larger magnetic charges than those that depend on spin-orbit coupling. The hexagonal manganites $RMnO_3$ and ferrites $RFeO_3$ ($R = Sc, Y, In, Ho-Lu$) exhibit strong couplings between electric, magnetic and structural degrees of freedom, with the transition-metal ions in the basal plane antiferromagnetically coupled through super-exchange so as to form a 120° noncollinear spin arrangement. Here we present a theoretical study of the magnetic charges, and of the spin-lattice and spin-electronic ME constants, in these hexagonal manganites and ferrites, clarifying the conditions under which exchange striction leads to an enhanced Z^m values and anomalously large in-plane spin-lattice ME effects.

PACS numbers: 75.85.+t, 75.30.Et, 75.70.Tj, 75.47.Lx

I. INTRODUCTION

The cross-coupling between magnetic, electric, and elastic properties can lead to a plethora of novel and profound physical phenomena, with potentially broad and innovative applications. Magnetoelectric (ME) effects are those in which the electric polarization \mathbf{P} responds to an applied magnetic field \mathbf{H} , or magnetization \mathbf{M} responds to an applied electric field \mathcal{E} . The ME coupling (MEC) between magnetic and electric properties has motivated intense experimental and theoretical investigations in bulk single crystals, thin films, composite layers, and organic-inorganic hybrid materials in recent years.^{1–11}

At the linear-response level, the linear MEC tensor α is defined as

$$\alpha_{\beta\nu} = \left. \frac{\partial P_\beta}{\partial H_\nu} \right|_{\mathcal{E}} = \mu_0 \left. \frac{\partial M_\nu}{\partial \mathcal{E}_\beta} \right|_{\mathbf{H}}, \quad (1)$$

where indices β and ν denote the Cartesian directions and μ_0 is the vacuum permeability. From a theoretical point of view, the linear ME effect can be decomposed into electronic (frozen-ion), ionic (lattice-mediated), and strain-mediated responses.¹¹ Each term can be further subdivided into spin and orbital contributions based on the origin of the induced magnetization. As the orbital moment is usually strongly quenched on the transition-metal sites, most phenomenological and first-principles studies have focused on the spin-electronic¹² and the spin-lattice^{13–15} contributions. The lattice response can be written, following Ref. 13, as

$$\alpha_{\beta\nu}^{\text{latt}} = \Omega_0^{-1} \mu_0 Z_{m\beta}^e (K^{-1})_{mn} Z_{n\nu}^m, \quad (2)$$

(sum over repeated indices implied), i.e., as a matrix product of the dynamical Born electric charge Z^e , the inverse force-constant matrix K^{-1} , and the dynamical

magnetic charge Z^m , where m and n are composite labels for an atom and its displacement direction. Ω_0 is the unit cell volume. Note that Z^m is the magnetic analog of the dynamical Born charge, and is defined as

$$Z_{m\nu}^m = \Omega_0 \left. \frac{\partial M_\nu}{\partial u_m} \right|_{\mathcal{E}, \mathbf{H}, \eta} = \mu_0^{-1} \left. \frac{\partial F_m}{\partial H_\nu} \right|_{\mathcal{E}, \mathbf{u}, \eta}, \quad (3)$$

where u_m is an internal displacement, F_m is an atomic force, and η is a homogeneous strain. In principle, Z^m has both spin and orbital parts, corresponding respectively to spin and orbital contributions to M_ν , or Zeeman and $\mathbf{p} \cdot \mathbf{A}$ terms induced by H_ν , but we shall focus on the spin part in the following. Our previous first-principles study has shown that exchange striction acting on noncollinear spin structures induces much larger magnetic charges than when Z^m is driven only by spin-orbit coupling (SOC). Therefore, exchange striction provides a promising mechanism for obtaining large MECs.¹⁶

The hexagonal manganites $RMnO_3$ and ferrites $RFeO_3$ ($R = Sc, Y, In, \text{ and } Ho-Lu$) form an interesting class of materials exhibiting strong couplings between electric, magnetic, and structural degrees of freedom.¹⁷ A series of first-principles^{15, 18–20} and phenomenological²¹ studies have greatly enhanced our understanding of the coupled properties. The ferroelectricity is induced by the structural trimerization, and the direction of the spontaneous polarization is related to the trimerization pattern.¹⁹ An interesting “cloverleaf” pattern formed from interlocking domain walls between structural and ferroelectric domains has been found in hexagonal $RMnO_3$ and is now understood in terms of Landau theory.^{21–23} Hexagonal $RMnO_3$ and $RFeO_3$ have rich magnetic phase diagrams and show considerable potential for manipulation and practical applications.^{24–26} The magnetic order has two different origins, with the transition-metal Mn^{3+} or Fe^{3+} sublattices ordering first, often followed by ordering of the rare-earth ions R^{3+} at lower temperature. The mag-

netic anisotropy is easy-plane and easy-axis for $3d$ and $4f$ spins respectively; the $3d$ moments are antiferromagnetically coupled through superexchange so as to form a 120° noncollinear arrangement in the x - y plane, while the $4f$ rare-earth moments are collinear along the hexagonal z axis.

The low-temperature magnetic phases of $RMnO_3$ and $RFeO_3$ allow a linear ME effect to be present. The recently developed ME force microscopy technique has been used successfully to observe the ME domains in $ErMnO_3$.²⁷ In that work, a large ME component $\alpha_{zz} \sim 13$ ps/m has been measured at 4 K, which is below the Mn^{3+} ordering temperature of 81 K but above the Er^{3+} ordering temperature of 2 K. However, first-principles calculations predict that the SOC-induced spin-lattice α_{zz} arising from the Mn^{3+} order is 0.7-1.0 ps/m.¹⁵ This discrepancy suggests that the dominant ME effect in the hexagonal \hat{z} direction is mediated by the Er^{3+} $4f$ electrons in $ErMnO_3$. The in-plane ME effect, which has not been measured or calculated, has a different origin. It is dominated by an exchange-striction mechanism on the Mn^{3+} sublattice, because the noncollinear spin pattern is sensitive to the lattice distortion. Thus, hexagonal $RMnO_3$ and $RFeO_3$ are good candidates to show exchange-striction enhanced magnetic charges and anomalously large spin-lattice MECs.

In this work, we use first-principles density-functional methods to study the magnetic charges and the spin-induced MECs arising from the $3d$ electrons in hexagonal $HoMnO_3$, $ErMnO_3$, $YbMnO_3$, $LuMnO_3$, and $LuFeO_3$. For the transverse magnetic charge components and MECs, we also provide a comparison between results induced solely by exchange striction and ones including SOC. Our results confirm that the exchange striction greatly enhances the in-plane magnetic charges, while the SOC contribution is minor for most components except on Mn atoms. However, the effect of SOC on the MECs is surprisingly large in many cases. This occurs because the exchange-striction contribution tends to be reduced by cancellations between modes, while the SOC contribution is mainly associated with a few low-frequency modes. The in-plane ME responses are discussed case by case, and the conditions under which exchange striction leads to anomalously large in-plane spin-lattice MECs are clarified.

The paper is organized as follows. In Sec. IIA and IIB we introduce the geometric structure and magnetic order of hexagonal $RMnO_3$ and $RFeO_3$. In Sec. IIC we analyze the tensor symmetries of the Born charges, magnetic charges and MECs in two different magnetic phases of $RMnO_3$ and $RFeO_3$. The computational details are described in Sec. IID. The results and discussion of Born charges, magnetic charges and MECs in $RMnO_3$ and $LuFeO_3$ are presented in Sec. III. We summarize and give our conclusions in Sec. IV.

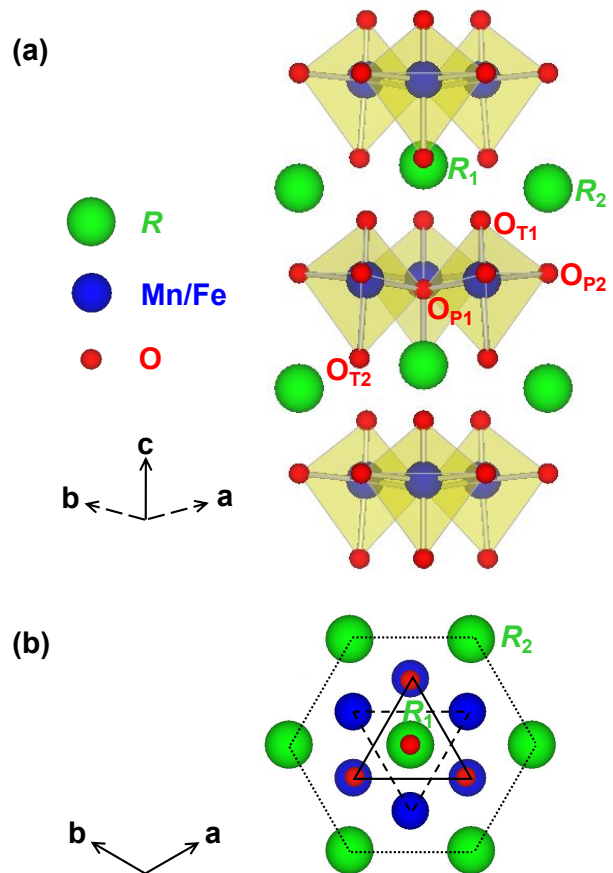


FIG. 1. Structure of ferroelectric hexagonal $RMnO_3$ (6 f.u. per primitive cell). (a) Side view from $[110]$. (b) Plan view from $[001]$; dashed (solid) triangle indicates three Mn^{3+} connected via Op_1 to form a triangular sublattice at $z = 0$ ($z = 1/2$).

II. PRELIMINARIES

A. Hexagonal $RMnO_3$

Above the structural transition temperature $T_c \sim 900$ - 1500 K, the hexagonal manganites $RMnO_3$ ($R = Sc, Y, In,$ and $Ho-Lu$) are paraelectric insulators. The space group is $P6_3/mmc$ with two formula units (f.u.) per primitive cell. Below T_c , the size mismatch between the small-radius R^{3+} ion and the large MnO_5 bipyramid leads to an inward tilting of the three corner-shared MnO_5 polyhedra and an associated “one-up/two-down” buckling of the R^{3+} ion layer, as shown in Fig. 1. The transition triples (“trimerizes”) the unit cell, lowers the structural symmetry to $P6_3cm$, and induces ferroelectricity. As the induced polarization is nonlinearly coupled to the trimerization, these systems are improper ferroelectrics.^{18,19,21}

The Mn^{3+} magnetic order develops below the Néel temperature T_N of ~ 70 - 130 K. The in-plane Mn-O-Mn

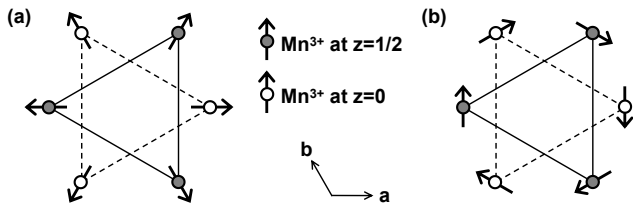


FIG. 2. Magnetic phases of hexagonal $RMnO_3$ and $RFeO_3$. Mn^{3+} ions form triangular sublattices at $z = 0$ (dash line) and $z = 1/2$ (solid line). (a) A_2 phase with magnetic symmetry $P6_3c'm'$; spins on a given Mn^{3+} layer point all in or all out. (b) A_1 phase with the magnetic symmetry $P6_3cm$, with Mn^{3+} spins pointing tangentially to form a vortex pattern. The A_1 and A_2 phases differ by a 90° global rotation of the spins. The B_1 and B_2 phases can be obtained from A_2 and A_1 by reversing the spins on the dashed triangles.

superexchange determines the noncollinear 120° antiferromagnetic (AFM) order on the Mn^{3+} triangular lattice. On the other hand, the inter-plane Mn-O-R-O-Mn exchange, which is two orders of magnitude weaker than the in-plane exchange, modulates the relative spin directions between two consecutive Mn planes.^{15,24} At temperatures lower than ~ 5.5 K, the rare-earth ions with partially filled $4f$ shells develop collinear spin order along the hexagonal z direction. For the Mn^{3+} order, there are four distinct magnetic phases, namely A_1 ($P6_3cm$), A_2 ($P6_3c'm'$), B_1 ($P6_3c'm'$), and B_2 ($P6_3c'm$). The linear ME effect exists only in A_1 and A_2 phases. The A_1 and A_2 phases are shown in Fig. 2; the B_1 and B_2 phases can be obtained from A_2 and A_1 by reversing the spins on the dashed triangles. From previous experiments, it is known that at zero temperature without a magnetic field, $HoMnO_3$ is in the A_1 phase, while $ErMnO_3$, $YbMnO_3$, and $LuMnO_3$ are not in either A phase. Under a weak magnetic field along the \hat{z} direction, $ErMnO_3$ and $YbMnO_3$ undergo a transition into the A_2 phase.²⁴⁻²⁶

B. Hexagonal $RFeO_3$

Epitaxially grown thin-film hexagonal $RFeO_3$ has a similar structure as hexagonal $RMnO_3$, with improper ferroelectricity below ~ 1000 K. Replacing Mn^{3+} with Fe^{3+} introduces larger spin moments and stronger superexchange interactions in the basal plane. In a recent experiment, AFM order has been found to develop at $T_N = 440$ K followed by a spin-reorientation transition below $T_R = 130$ K in $LuFeO_3$.²⁸ It has also been confirmed that below 5 K, the magnetic structure of $LuFeO_3$ is that of the A_2 phase.²⁹

C. Symmetry

Our purpose is to understand the mechanisms that generate large magnetic charges that may in turn in-

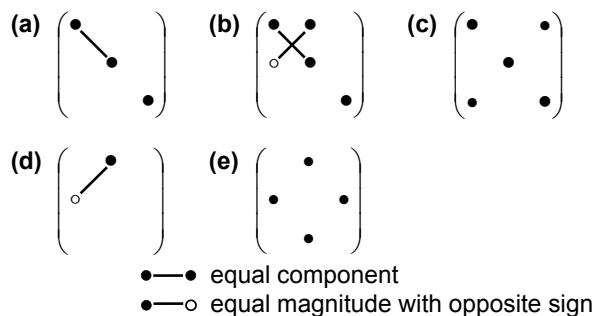


FIG. 3. Symmetry patterns of Born charges, magnetic charges and ME tensors in $RMnO_3$ and $RFeO_3$. (a) Tensor form of the ME coupling in the A_2 phase, Born charges on R_1 and OP_1 sites in either A phase, and magnetic charges on the same sites in the A_2 phase. (b) Tensor form of the Born and magnetic charges on R_2 and OP_2 sites in either A phase. (c) Tensor form of the Born charges on Mn, Fe, OT_1 , and OT_2 sites lying on an M_y mirror plane in either A phase, and of the magnetic charges on the same sites in the A_2 phase. (d) Tensor form of the ME coupling in the A_1 phase, and of the magnetic charges on R_1 and OP_1 sites in the A_1 phase. (e) Tensor form of the magnetic charges on Mn, Fe, OT_1 , and OT_2 sites lying on an M_y mirror plane in the A_1 phase.

duce anomalously large spin-lattice MECs. Therefore, we focus on the A_1 and A_2 magnetic phases, shown in Fig. 2, which allow a linear MEC to exist. $ErMnO_3$, $YbMnO_3$, and $LuMnO_3$ actually adopt other phases as their ground-state magnetic order at low temperature. Nevertheless, we include them for purposes of comparison when calculating the properties of the hexagonal $RMnO_3$ materials in the A_2 phase. We also study $LuFeO_3$ in the A_2 phase, and for $HoMnO_3$ we study both the A_1 and A_2 phases.

The A_1 and A_2 phases have the same $P6_3cm$ structural symmetry, so the forms of the atomic Born charge tensors in the two phases are the same. The Born charges for R_1 and OP_1 take the tensor form shown in Fig. 3(a), while those of R_2 and OP_2 have the symmetry pattern shown in Fig. 3(b). For the Mn, Fe, OT_1 , and OT_2 sites lying on a vertical M_y mirror plane, the Born charges are as given in Fig. 3(c); for the partner sites related by rotational symmetry, the tensors also need to be rotated accordingly.

The symmetry forms of the atomic magnetic charge tensors can be derived from the on-site magnetic point symmetries. For the A_1 phase, the magnetic space group is $P6_3cm$ and the magnetic charges of R_1 and OP_1 take the forms given in Fig. 3(d); those for R_2 and OP_2 have the tensor symmetry shown in Fig. 3(b); and for Mn, Fe, OT_1 , and OT_2 they can be written in the form of Fig. 3(e). For the A_2 phase, the magnetic group is $P6_3c'm'$; all the improper operators are associated with the time-reversal operation, so the magnetic charges have the same tensor forms as the Born charges.

A symmetry analysis of the structure and the mag-

TABLE I. Atomic Born charge tensors Z^e (in units of $|e|$) for LuMnO_3 and LuFeO_3 in the A_2 phase. TM = Mn or Fe.

	LuMnO_3	LuFeO_3		LuMnO_3	LuFeO_3
$Z_{xx}^e(\text{Lu}_1)$	3.61	3.79	$Z_{xz}^e(\text{OT}_1)$	0.19	0.11
$Z_{zz}^e(\text{Lu}_1)$	4.12	3.94	$Z_{zz}^e(\text{OT}_1)$	-3.19	-3.21
$Z_{xx}^e(\text{Lu}_2)$	3.66	3.84	$Z_{xx}^e(\text{OT}_2)$	-1.90	-2.15
$Z_{yx}^e(\text{Lu}_2)$	0.13	0.15	$Z_{xx}^e(\text{OT}_2)$	-0.20	-0.19
$Z_{zz}^e(\text{Lu}_2)$	3.96	3.88	$Z_{yy}^e(\text{OT}_2)$	-1.85	-2.13
$Z_{xx}^e(\text{TM})$	3.17	2.96	$Z_{xz}^e(\text{OT}_2)$	-0.18	-0.11
$Z_{zz}^e(\text{TM})$	0.44	0.21	$Z_{zz}^e(\text{OT}_2)$	-3.33	-3.30
$Z_{yy}^e(\text{TM})$	3.26	3.01	$Z_{xx}^e(\text{OP}_1)$	-3.00	-2.40
$Z_{zz}^e(\text{TM})$	0.07	-0.02	$Z_{zz}^e(\text{OP}_1)$	-1.54	-1.61
$Z_{zz}^e(\text{TM})$	3.95	4.16	$Z_{xx}^e(\text{OP}_2)$	-3.05	-2.45
$Z_{xx}^e(\text{OT}_1)$	-1.92	-2.19	$Z_{yx}^e(\text{OP}_2)$	-0.03	-0.02
$Z_{zz}^e(\text{OT}_1)$	0.25	0.25	$Z_{zz}^e(\text{OP}_2)$	-1.43	-1.52
$Z_{yy}^e(\text{OT}_1)$	-2.00	-2.28			

netic space group identifies the phonon modes that couple to the electromagnetic field. The infrared (IR)-active phonon modes that couple to the electric field are the longitudinal A_1 modes and the transverse E_1 modes,

$$\Gamma_{\text{IR}} = 10A_1 + 15E_1, \quad (4)$$

including the three acoustic modes. The magnetization is generated by phonon modes that couple to the magnetic field. In the A_1 phase, the magneto-active phonon modes are the longitudinal A_2 modes and the transverse E_1 modes,

$$\Gamma_{\text{mag}}^{A_1} = 5A_2 + 15E_1, \quad (5)$$

where one pair of acoustic E_1 modes are included. In the A_2 phase, on the other hand, the IR- and magneto-active phonon modes are identical, since the magnetic and Born charge tensors have the same form in this case.

For the MECs in the A_1 phase, as the longitudinal IR-active and magneto-active modes are mutually exclusive, the ME tensor takes the form of Fig. 3(d), which does not have a longitudinal ME component. For the A_2 magnetic phase, the A_1 and E_1 modes are both IR-active and magneto-active, so that the ME tensor has both longitudinal and transverse components and adopts the form shown in Fig. 3(a).

D. First-principles methods

Our calculations are performed with plane-wave density functional theory (DFT) implemented in VASP³⁰ using the generalized-gradient approximation parametrized by the Perdew-Burke-Ernzerhof functional.³¹ The ionic core environment is simulated by projector augmented wave (PAW) pseudopotentials,³² and the $4f$ electrons are placed in the PAW core. We use a Hubbard $U = 4.5$ eV and $J = 0.95$ eV on the d orbitals of the Mn/Fe atoms, and the moment on the rare-earth ions are not

TABLE II. Eigenvalues of the force-constants matrix ($\text{eV}/\text{\AA}^2$) for IR-active modes in LuMnO_3 and LuFeO_3 in the A_2 phase, excluding translational modes.

A_1 modes		E_1 modes	
LuMnO_3	LuFeO_3	LuMnO_3	LuFeO_3
4.24	3.48	3.32	3.56
7.44	6.70	4.68	4.62
8.74	8.41	6.73	6.97
11.51	11.47	7.35	8.09
14.01	12.03	8.63	8.83
15.60	15.59	9.56	9.24
22.66	20.53	11.36	11.37
25.87	22.83	12.46	12.46
35.82	28.46	13.02	13.85
		14.09	14.92
		16.49	16.87
		17.37	17.35
		23.36	21.19
		37.75	28.75

considered.¹⁵ The structures are fully relaxed in the DFT+ U ³³ calculations with their non-collinear spin arrangements in two cases, when SOC is present and when it is absent. In our noncollinear magnetization calculation, a high cutoff energy 700 eV and a tight energy error threshold 1.0×10^{-9} eV are necessary to get fully converged magnetic properties. The Born effective charge tensors and the Γ -point force-constant matrices are obtained using linear-response methods in the absence of SOC. The dynamical magnetic charges are computed by applying a uniform Zeeman field¹² to the crystal and computing the resulting forces. Polarization is calculated using the Berry phase formalism.³⁴ A $4 \times 4 \times 2$ Γ -centered k -point mesh is used in the calculations.

III. RESULTS AND DISCUSSION

A. Born charge and force-constant matrix

The f electrons are not included in our calculations for the hexagonal $RMnO_3$ class of materials, so the major differences between compounds result from the variation of the rare-earth radius; the trimerization tends to increase as the radius of the rare-earth element decreases. Because of the similarity in the geometric structures, the dielectric and phonon properties are almost identical in the $RMnO_3$ compounds, regardless of the magnetic ordering. In Tables I and II we list the Born charge tensors and the eigenvalues of the force-constant matrix for the IR-active modes of LuMnO_3 and LuFeO_3 . Only small differences are observed between LuMnO_3 and LuFeO_3 , reflecting the different transition-metal atom. The results for the other $RMnO_3$ compounds are quite similar to those of LuMnO_3 and are given for completeness in the Supplement.

TABLE III. Longitudinal magnetic charge components Z^m ($10^{-3}\mu_B/\text{\AA}$) of $RMnO_3$ and $LuFeO_3$ in the A_2 phase. All components vanish in the absence of SOC.

	HoMnO ₃	ErMnO ₃	YbMnO ₃	LuMnO ₃	LuFeO ₃
$Z_{zz}^m(R_1)$	-50	-53	-53	-67	7
$Z_{zz}^m(R_2)$	14	35	24	16	7
$Z_{zz}^m(TM)$	-92	-86	-61	-67	9
$Z_{zz}^m(TM)$	24	1	6	25	2
$Z_{xz}^m(O_{T1})$	-49	-44	-41	-19	23
$Z_{zz}^m(O_{T1})$	99	81	53	33	22
$Z_{xz}^m(O_{T2})$	-7	-12	-12	-12	0
$Z_{zz}^m(O_{T2})$	-119	-94	-64	-49	-25
$Z_{zz}^m(O_{P1})$	-276	-257	-230	-190	54
$Z_{zz}^m(O_{P2})$	141	140	125	100	-35

B. Magnetization and magnetic charge

In the A_2 phase, the trimerization induces not only an electric polarization, but also a weak ferromagnetism in the \hat{z} direction arising from out-of-plane tilting of the Mn^{3+} spin moments induced by SOC. The net magnetizations in the 30-atom unit cell for A_2 -phase HoMnO₃, ErMnO₃, YbMnO₃, and LuMnO₃ are 0.309, 0.303, 0.292, and 0.268 μ_B , respectively. These magnetic moments are found to depend almost linearly on the tilting angle of the MnO_5 bipyramids, which takes values of 5.03°, 5.07°, 5.16°, and 5.21° respectively in these four compounds, but in any case the variation is not very large. In contrast, the result for LuFeO₃ is -0.077 μ_B , which is much smaller and of opposite sign compared with the $RMnO_3$ materials.

The magnetic charges defined in Eq. (3) are more sensitive to the local environment, and now the differences between $RMnO_3$ compounds are more significant. We divide the magnetic charge components into two groups that we label as “longitudinal” and “transverse” depending on whether the coupling is to magnetic fields along the \hat{z} direction or in the x - y plane respectively.⁷

The longitudinal magnetic charge components are calculated with a magnetic field directed along \hat{z} , which is roughly perpendicular to the spin directions. These components are only non-zero when SOC is considered. The scenario here is similar to the case of a transverse magnetic field (H_x or H_y) applied to Cr_2O_3 , since the magnetization is along the z axis for Cr_2O_3 . It is therefore not surprising to find that the longitudinal magnetic charges of $RMnO_3$ and $LuFeO_3$ in Table III are comparable to the SOC-induced transverse magnetic charges in Cr_2O_3 .¹⁶ The longitudinal magnetic charges for O_{P1} and O_{P2} in $LuFeO_3$ are opposite to, and about three times smaller than, the ones in $RMnO_3$. These results explain the differences between $RMnO_3$ and $LuFeO_3$ regarding the magnitude and the direction of the weak ferromagnetism, which is generated by trimerization distortions involving vertical displacements of O_{P1} and O_{P2} .

For the response to transverse magnetic fields, both

TABLE IV. Transverse magnetic charge components Z^m ($10^{-2}\mu_B/\text{\AA}$) of HoMnO₃ in the A_1 phase, as computed including or excluding SOC.

	Total	No SOC	Total	No SOC	
$Z_{yx}^m(Ho_1)$	-25	-28	$Z_{zy}^m(O_{T1})$	-188	-230
$Z_{xx}^m(Ho_2)$	-15	-18	$Z_{yx}^m(O_{T2})$	-57	-67
$Z_{yx}^m(Ho_2)$	-1	3	$Z_{xy}^m(O_{T2})$	-20	-26
$Z_{yx}^m(Mn)$	92	54	$Z_{zy}^m(O_{T2})$	-192	-231
$Z_{xy}^m(Mn)$	-10	2	$Z_{yx}^m(O_{P1})$	-483	-551
$Z_{zy}^m(Mn)$	41	48	$Z_{xx}^m(O_{P2})$	395	461
$Z_{yx}^m(O_{T1})$	23	28	$Z_{yx}^m(O_{P2})$	184	253
$Z_{xy}^m(O_{T1})$	-7	-7			

the field and the spins lie in the basal plane, so the dynamical magnetic charges are driven by both SOC and exchange striction. As the exchange-striction strength can exceed that of the SOC by orders of magnitude in some materials, it is worthwhile to understand the relative size of these two effects in $RMnO_3$ and $LuFeO_3$. In Tables IV and V we present the transverse magnetic charges induced with and without SOC in the A_1 and A_2 phases. It is obvious that the SOC contributions are an order of magnitude smaller for many transverse components. Similarly, the magnetic charges induced by exchange striction are about ten times larger than the SOC-driven longitudinal ones in Table III. However, the SOC is crucial for the Mn atoms and it even reverses the signs of their transverse magnetic charges.

C. Magnetoelectric effect

We calculate the spin-lattice MEC from Eq. (2) using our computed Born charges, force-constant matrices, and magnetic charges. The spin-electronic contributions are calculated based on the $\partial P/\partial H$ version of Eq. (1) with the lattice degrees of freedom frozen. We further subdivide the ME tensor components into longitudinal and transverse ones based on the direction of \mathbf{H} relative to the hexagonal axis as before, so that the longitudinal (transverse) spin-lattice MEC is calculated using the longitudinal (transverse) magnetic charge components. The MEC tensor elements allowed by symmetry are the longitudinal α_{zz} and transverse $\alpha_{xx} = \alpha_{yy}$ ones in the A_2 phase, and only the transverse $\alpha_{yx} = -\alpha_{xy}$ components in the A_1 phase.

In the first part of Table VI, the spin-contributed longitudinal MECs are shown for $RMnO_3$ and $LuFeO_3$ in the A_2 phase. The MEC from the spin channel is dominated by the spin-lattice contribution. Although the longitudinal magnetic charges of $LuFeO_3$ are smaller than for $RMnO_3$, the spin-lattice MECs $|\alpha_{zz}|$ in $RMnO_3$ and $LuFeO_3$ are similar, ~ 0.25 ps/m. The results are comparable to those reported for the transverse MEC in Cr_2O_3 ³⁵ and for α_{zz} in $ErMnO_3$ ¹⁵ in previous first-principles calculations. In the second part of Table VI, we

TABLE V. Transverse magnetic charge components Z^m ($10^{-2}\mu_B/\text{\AA}$) of $RMnO_3$ and $LuFeO_3$ in the A_2 phase, as computed including or excluding SOC.

	HoMnO ₃		ErMnO ₃		YbMnO ₃		LuMnO ₃		LuFeO ₃	
	Total	No SOC	Total	No SOC	Total	No SOC	Total	No SOC	Total	No SOC
$Z_{xx}^m(R_1)$	-23	-24	-21	-22	-37	-40	-42	-35	-36	-52
$Z_{xx}^m(R_2)$	6	-1	6	3	12	9	14	6	15	24
$Z_{yx}^m(R_2)$	16	18	11	12	10	10	8	7	-9	-11
$Z_{xx}^m(TM)$	-2	10	-7	-10	-16	-21	-11	1	-52	-43
$Z_{zx}^m(TM)$	-42	-24	-38	-22	-25	-34	-31	-17	-102	-95
$Z_{yy}^m(TM)$	-5	46	-7	32	-22	27	-32	15	-16	-11
$Z_{xx}^m(O_{T1})$	5	5	6	6	12	16	14	11	0	0
$Z_{zx}^m(O_{T1})$	191	221	150	154	162	178	150	122	128	105
$Z_{yy}^m(O_{T1})$	24	23	22	22	31	33	34	25	15	11
$Z_{xx}^m(O_{T2})$	20	23	16	19	19	22	17	12	25	20
$Z_{zx}^m(O_{T2})$	195	217	140	161	173	189	166	134	130	110
$Z_{yy}^m(O_{T2})$	-59	-61	-48	-46	-57	-60	-57	-45	-41	-42
$Z_{xx}^m(OP_1)$	-445	-510	-392	-422	-532	-602	-564	-499	-665	-609
$Z_{xx}^m(OP_2)$	241	234	215	202	298	299	316	247	388	356
$Z_{yx}^m(OP_2)$	-378	-422	-335	-355	-466	-506	-498	-427	-673	-621

show the spin-related transverse MECs α_{xx} for $RMnO_3$ and $LuFeO_3$ in the A_2 phase. The same information is presented in graphical form in Fig. 4.

It is clear from the comparison between the first and second parts of Table VI that the transverse spin-lattice MECs are one order of magnitude larger than the longitudinal ones, as a result of the exchange-striction mechanism. Surprisingly, Fig. 4(a) shows that the effect of SOC on the exchange striction is profound, even reversing the sign of the spin-lattice MECs in $RMnO_3$. This unusual behavior can be traced mainly to two observations about the spin-lattice contributions from different IR-active modes in the $RMnO_3$ materials. Firstly, the

exchange-striction MEC is smaller than expected as a result of a large degree of cancellation between the contributions from different transverse IR-active modes. To illustrate this, the mode-by-mode contributions are presented for a few selected cases in Table VII. Secondly, the softest modes are dominated by Mn displacements, precisely those for which SOC has the largest effect on the Z^m values, even flipping the sign of some components. In

TABLE VI. Computed MECs α_{zz} (longitudinal) and α_{xx} and α_{yx} (transverse) for $RMnO_3$ and $LuFeO_3$ (ps/m). Spin-lattice, spin-electronic, and total spin couplings are given as computed with and without SOC.

	Spin-latt.		Spin-elec.		Total spin	
	Total	No SOC	Total	No SOC	Total	No SOC
	α_{zz} in A_2 phase					
HoMnO ₃	-0.27	0	0.06	0	-0.21	0
ErMnO ₃	-0.26	0	0.05	0	-0.21	0
YbMnO ₃	-0.25	0	0.06	0	-0.19	0
LuMnO ₃	-0.19	0	0.00	0	-0.19	0
LuFeO ₃	0.26	0	0.00	0	0.26	0
	α_{xx} in A_2 phase					
HoMnO ₃	-0.99	5.12	4.10	4.83	3.11	9.95
ErMnO ₃	-1.30	2.40	2.56	3.72	1.26	6.12
YbMnO ₃	-2.52	1.20	3.72	4.66	1.20	5.86
LuMnO ₃	-2.60	1.31	3.82	3.50	1.22	4.81
LuFeO ₃	-2.20	-1.57	-0.79	-0.32	-2.99	-1.89
	α_{yx} in A_1 phase					
HoMnO ₃	9.55	4.88	5.24	5.35	14.79	10.23

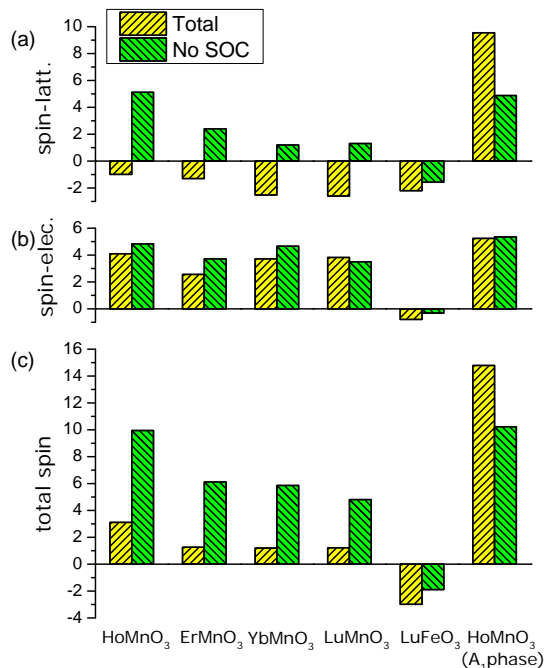


FIG. 4. Transverse MECs for $RMnO_3$ and $LuFeO_3$. α_{xx} (ps/m) in the A_2 phase and α_{yx} in the A_1 phase. (a) Spin-lattice; (b) spin-electronic; and (c) total spin couplings.

TABLE VII. Transverse MEC contributions (ps/m) from IR-active modes for A_2 and A_1 phases of HoMnO_3 and A_2 phase of LuMnO_3 . Results are given in ascending order of force-constant eigenvalues, which are reported in Table II of the Supplement.

A_2 phase HoMnO_3		A_1 phase HoMnO_3		A_2 phase LuFeO_3	
Total	No SOC	Total	No SOC	Total	No SOC
0.01	0.12	0.25	0.18	0.28	0.39
-1.16	2.62	4.98	2.36	-0.54	-0.50
0.66	2.32	3.59	2.37	-1.31	-1.22
-0.51	-0.35	-0.32	-0.48	1.30	1.23
2.79	3.13	2.87	3.33	3.31	3.12
0.35	0.21	0.30	0.30	1.84	1.73
-1.88	-1.85	-1.35	-1.90	-4.43	-4.11
1.13	1.25	1.19	1.38	-2.59	-2.25
-2.96	-3.07	-2.70	-3.40	1.24	1.13
0.01	0.13	0.19	0.06	-1.48	-1.27
0.21	0.24	0.21	0.26	-0.15	-0.14
0.36	0.40	0.34	0.42	0.89	0.83
-0.03	-0.03	-0.03	-0.04	-0.62	-0.55
0.02	0.01	0.03	0.03	0.07	0.03

this way, it turns out that SOC can result in large relative changes in the MEC results. In the case of LuFeO_3 , the SOC effect on the Z^m values is weak, even for Fe atoms. Thus, the MEC of LuFeO_3 does not change as dramatically as that of RMnO_3 when SOC is included.

From Fig. 4(b) it can be seen that the spin-electronic contribution is not negligible in the transverse direction, and it counteracts the MEC from the spin-lattice channel in A_2 phase RMnO_3 . The total transverse ME effect is summarized in Fig. 4(c). Because of the large SOC effect and the cancellation between the lattice and electronic contributions, the total spin MEC α_{xx} is ~ 1.2 ps/m in most A_2 -phase RMnO_3 compounds, except for HoMnO_3 . In HoMnO_3 , the cancellation between the spin-lattice and the spin-electronic MECs is the weakest of all the RMnO_3 compounds, resulting in the largest total spin MEC of ~ 3.1 ps/m in the A_2 phase. In LuFeO_3 , the spin-lattice and spin-electronic terms are all smaller than in RMnO_3 . However, the cancellation induced by the SOC perturbation and the spin-electronic contribution is avoided, so that LuFeO_3 has a large total spin MEC of ~ -3 ps/m.

We present the MECs for HoMnO_3 in the A_1 phase in

the last line of Table VI and in Fig. 4. In principle the MECs of HoMnO_3 in the A_1 and A_2 phases should be the same without SOC, as the two phases only differ by a global spin rotation. This is approximately confirmed by a comparison of the corresponding entries for HoMnO_3 in Table VI. The ME contribution from exchange striction (i.e., without SOC) is ~ 5 ps/m for both the A_2 and A_1 phases. However, when the effect of SOC is included, the spin-lattice contribution is strongly enhanced by another ~ 5 ps/m. Furthermore, the spin-electronic MEC has the same sign as the spin-lattice one, which adds ~ 5 ps/m to the MEC. Therefore, the total spin MEC α_{yx} reaches ~ 15 ps/m, and is the largest in all of the RMnO_3 and LuMnO_3 materials we studied.

IV. SUMMARY

In summary, we have studied the spin-related magnetic charges and MECs for HoMnO_3 , ErMnO_3 , YbMnO_3 , LuMnO_3 , and LuFeO_3 using first-principles calculations. We confirm that the exchange striction acting on non-collinear spins induces much larger magnetic charges than does SOC acting alone. Nevertheless, the effect of SOC on the MECs is surprisingly large, rivaling that of exchange striction in many cases. This occurs because the exchange-striction contribution tends to be reduced by cancellations between different IR-active modes, while the SOC contribution is mainly associated with just a few low-frequency modes with large Mn displacements. We also find that the RMnO_3 materials have spin-electronic MECs comparable to the spin-lattice ones. Among the RMnO_3 and LuFeO_3 materials we studied, we find that the A_1 phase of HoMnO_3 is the most promising ME material, with the largest MEC of ~ 15 ps/m. Extrapolating our conclusions to other hexagonal RMnO_3 and RFeO_3 compounds that are not included in our calculations, we predict that the A_2 phase is more promising for the ferrites, while the A_1 phase has a stronger MEC for the manganites.

ACKNOWLEDGMENTS

We thank Weida Wu for useful discussions. The work was supported by ONR grant N00014-12-1-1035.

* mengye@physics.rutgers.edu

¹ M. Fiebig, J. Phys. D **38**, R123 (2005).

² N. A. Spaldin and M. Fiebig, Science **309**, 391 (2005).

³ W. Eerenstein, N. D. Mathur and J. F. Scott, Nature **442**, 759 (2006).

⁴ Y. Tokura, J. Magn. Magn. Mater. **310** 1145 (2007).

⁵ S.-W. Cheong and M. Mostovoy, Nat. Mater. **6**, 13 (2007).

⁶ R. Ramesh and N. A. Spaldin, Nat. Mater. **6**, 21 (2007).

⁷ K. F. Wang, J.-M. Liu and Z. F. Ren, Adv. Phys. **58**, 321 (2009).

⁸ M. Fiebig and N. A. Spaldin, Eur. Phys. J. B **71**, 293 (2009).

⁹ J.-P. Rivera, Eur. Phys. J. B **71**, 299 (2009).

¹⁰ D. Khomskii, Physics **2**, 20 (2009).

¹¹ T. Birol, N. A. Benedek, H. Das, A. L. Wysocki, A. T. Mulder, B. M. Abbett, E. H. Smith, S. Ghosh, and C. J.

- Fennie, *Curr. Opin. Solid State Mater. Sci.* **16**, 227 (2012).
- ¹² E. Bousquet, N. A. Spaldin, and K. T. Delaney, *Phys. Rev. Lett.* **106**, 107202 (2011).
- ¹³ J. Íñiguez, *Phys. Rev. Lett.* **101**, 117201 (2008).
- ¹⁴ K. T. Delaney, M. Mostovoy and N. A. Spaldin, *Phys. Rev. Lett.* **102**, 157203 (2009).
- ¹⁵ H. Das, A. L. Wysocki, Y. Geng, W. Wu and C. J. Fennie, *Nat. Commun.* **5**, 2998 (2014).
- ¹⁶ M. Ye and D. Vanderbilt, *Phys. Rev. B* **89**, 064301 (2014).
- ¹⁷ M. Mostovoy, *Nat. Mater.* **9**, 188 (2010).
- ¹⁸ B. B. Van Aken, T. T. M. Palstra, A. Filippetti and N. A. Spaldin, *Nat. Mater.* **3**, 164 (2004).
- ¹⁹ C. J. Fennie and K. M. Rabe, *Phys. Rev. B* **72**, 100103 (2005).
- ²⁰ Y. Kumagai and N. A. Spaldin, *Nat. Commun.* **4**, 1540 (2013).
- ²¹ S. Artyukhin, K. T. Delaney, N. A. Spaldin and M. Mostovoy, *Nat. Mater.* **13**, 42 (2013).
- ²² T. Choi, Y. Horibe, H. T. Yi, Y. J. Choi, W. Wu and S.-W. Cheong, *Nat. Mater.* **9**, 253 (2010).
- ²³ S.-Z. Lin, X. Wang, Y. Kamiya, G.-W. Chern, F. Fan, D. Fan, B. Casas, Y. Liu, V. Kiryukhin, W. H. Zurek, C. D. Batista and S.-W. Cheong, *Nature Phys.* **10**, 970 (2014).
- ²⁴ M. Fiebig, Th. Lottermoser and R. V. Pisarev, *J. Appl. Phys.* **93**, 8194 (2003).
- ²⁵ F. Yen, C. D. Cruz, B. Lorenz, E. Galstyan, Y. Y. Sun, J. B. Lorenz, *ISRN Condens. Matter Phys.* **2013**, 43 (2013).
- ²⁷ Y. Geng, H. Das, A. L. Wysocki, X. Wang, S.-W. Cheong, M. Mostovoy, C. J. Fennie and W. Wu, *Nat. Mater.* **13**, 163 (2014).
- ²⁸ W. Wang, J. Zhao, W. Wang, Z. Gai, N. Balke, M. Chi, H. N. Lee, W. Tian, L. Zhu, X. Cheng, D. J. Keavney, J. Yi, T. Z. Ward, P. C. Snijders, H. M. Christen, W. Wu, J. Shen and X. Xu, *Phys. Rev. Lett.* **110**, 237601 (2013).
- ²⁹ S. M. Disseler, J. A. Borchers, C. M. Brooks, J. A. Mundy, J. A. Moyer, D. A. Hillsberry, E. L. Thies, D. A. Tenne, J. Heron, J. D. Clarkson, G. M. Stiehl, P. Schiffer, D. A. Muller, D. G. Schlom, W. D. Ratcliff, arXiv:1411.1694 (2014).
- ³⁰ G. Kresse and J. Furthmüller, *Phys. Rev. B* **54**, 11169 (1996).
- ³¹ J. P. Perdew, K. Burke, and M. Ernzerhof, *Phys. Rev. Lett.* **77**, 3865 (1996).
- ³² P. E. Blochl, *Phys. Rev. B* **50**, 17953(1994); G. Kresse and D. Joubert, *Phys. Rev. B* **59**, 1758 (1999).
- ³³ A. I. Liechtenstein, V. I. Anisimov, and J. Zaanen, *Phys. Rev. B* **52**, R5467 (1995)
- ³⁴ R. D. King-Smith and D. Vanderbilt, *Phys. Rev. B* **47**, 1651 (1993).
- ³⁵ A. Malashevich, S. Coh, I. Souza and D. Vanderbilt, *Phys. Rev. B* **86**, 094430 (2012).